Geochemistry, Geophysics, Geosystems®

AGU ADVANCING EARTH AND SPACE SCIENCES

RESEARCH ARTICLE
10.1029/2024GC011778

Geochemical and Thermal Constraints on the Hikurangi Subduction Zone Hydrogeologic System and Its Role in Slow Slip

I. Aylward[1], E. A. Solomon[1], M. E. Torres[2], and R. N. Harris[2]

[1]School of Oceanography, University of Washington, Seattle, WA, USA, [2]College of Earth, Ocean, and Atmospheric Sciences, Oregon State University, Corvallis, OR, USA

Key Points:

- Pore water geochemistry and heat flow at seeps along the Hikurangi margin indicate shallow fluid sources and low fluid flow rates
- Fault zones hosting the sampled seeps are likely characterized by low permeability at depth
- Inefficient fluid drainage may lead to high pore fluid pressures along the plate boundary and influence the timing and mode of fault slip

Supporting Information:

Supporting Information may be found in the online version of this article.

Correspondence to:

I. Aylward and E. A. Solomon,
iaylward@uw.edu;
esolomn@uw.edu

Citation:

Aylward, I., Solomon, E. A., Torres, M. E., & Harris, R. N. (2025). Geochemical and thermal constraints on the Hikurangi subduction zone hydrogeologic system and its role in slow slip. *Geochemistry, Geophysics, Geosystems*, *26*, e2024GC011778. https://doi.org/10.1029/2024GC011778

Received 22 JUL 2024
Accepted 31 JAN 2025

Abstract Fluid generation and migration regulate the development of pore fluid pressure, which is hypothesized to influence the occurrence of slow slip events at subduction zones. Seafloor seep sites present the opportunity to directly sample fluids flowing through the accretionary wedge and assess the hydrogeologic conditions of the outer forearc. We present heat flow measurements and pore water geochemistry from sediment cores collected at fault-hosted seep sites on the southern and northern Hikurangi margin, offshore the North Island of New Zealand. These measurements span the deformation front to the shelf break. Along the northern margin, heat flow data do not show anomalies that can be obviously attributed to the discharge of warm fluids. Pore fluid compositions indicate that seep fluids originate from compaction within the uppermost wedge. Reactive-transport modeling of pore water solute profiles produces fluid flow rate estimates ≤2 cm/yr. Shallow fluid sources and low discharge rates at offshore fault-hosted seeps suggest that the sampled fault zones are characterized by low permeability at depth, preventing efficient drainage of the megathrust and underthrust sediments to the seafloor. These results provide additional evidence that the northern Hikurangi margin plate boundary is associated with high pore fluid pressures that likely act as a control on slow slip activity.

Plain Language Summary Subduction zone faults can produce devastating earthquakes and tsunamis when tectonic plates slip quickly past one another. The plate boundary (sometimes called the megathrust) can also slip slowly without generating seismic shaking during slow slip events. The magnitude of pore fluid pressure along the megathrust and in the surrounding sediments, controlled in part by the ability or inability of fluids to drain from the megathrust zone, is thought to impact the occurrence of fast versus slow slip. We investigate fluid drainage along the Hikurangi subduction zone offshore of New Zealand by sampling seafloor seeps, locations where fluids channeled along fault zones are expelled at the seafloor. Our heat flow and pore fluid geochemistry results suggest that fluids expelled at the sampled seeps are sourced from shallow sediment depths and are discharging at relatively low rates. We find no evidence that fault zones offshore of the southern and northern Hikurangi margin allow efficient drainage of fluids from deep within the subduction zone to the seafloor. These results support the hypothesis that high pore fluid pressures exist along the megathrust and in surrounding sediments, likely influencing the timing and style of fault slip.

1. Introduction

Geodetic and seismological observations at subduction zones over the last few decades have revealed a range of modes by which stress is released on the plate boundary, including episodic slow slip events (SSEs). SSEs occur at rates intermediate between fast, seismic slip that generates earthquakes (centimeters to meters per second) and aseismic creep at plate motion rates (centimeters per year) (e.g., Dragert et al., 2001; Hirose et al., 1999; Peng & Gomberg, 2010; Sacks et al., 1978; Schwartz & Rokosky, 2007). Offshore the east coast of New Zealand's North Island, where the Pacific plate subducts beneath the Australian plate, the Hikurangi subduction zone (HSZ) hosts frequent, well-studied SSEs (Wallace, 2020 and references therein). The southern Hikurangi margin is characterized by deep (>30 km), long (>1 year), infrequent SSEs (every ~5 years) that occur at the thermally controlled down-dip transition from brittle to ductile behavior (McCaffrey et al., 2008; Wallace, 2020). In contrast, the northern margin exhibits shallow (<15 km), short (<~1 month), frequent events (every 1–2 years) (Wallace, 2020). It is hypothesized that shallow SSEs in the northern HSZ are enabled by conditional fault zone stability arising from low effective normal stress linked to elevated pore fluid pressure (e.g., Bangs et al., 2023; Bell et al., 2010; Gase et al., 2023; Saffer & Wallace, 2015; Warren-Smith et al., 2019). Thus, characterizing the

pore fluid pressure distribution in the source region of slow slip is recognized as an important step toward understanding SSEs and subduction zone fault behavior (e.g., Arnulf et al., 2021; Bell et al., 2010; Ellis et al., 2015; Sun et al., 2020a).

The development of pore fluid pressure in marine sediments is regulated by the balance of fluid sources (inputs) and fluid flow (outputs). Pore fluid overpressure (i.e., pore fluid pressure in excess of hydrostatic pressure) is common in subduction zones due to rapid mechanical loading of sediment and the release of mineral bound water that outpace drainage through low permeability matrix sediments (e.g., Ellis et al., 2015; Gamage & Screaton, 2006; Ranero et al., 2008; Sun et al., 2020a). Elevated pore fluid pressure reduces effective normal stress, which in turn reduces fault strength and can promote conditions favorable for slow slip. However, the plate boundary and faults within the forearc often exhibit higher permeability than the matrix sediments, thereby providing pathways for focused fluid flow and drainage of both underthrust and wedge sediments (e.g., Moore et al., 1991; Moore & Vrolijk, 1992; Saffer & Tobin, 2011). Drainage of fluids along fault zones relieves overpressure, leading to an increase in effective stress and fault strength, which can promote stick-slip behavior. Thus, the pore pressure distribution, and its contribution to fault strength and stability, along the plate boundary are dictated by fluid sources and the permeability of the plate boundary and wedge, that is, the ability of faults to support appreciable rates of fluid flow (e.g., Lauer & Saffer, 2012; Saffer & Bekins, 1998; Sun et al., 2020a).

Seep sites on the outer forearc of subduction zones often coincide with faults that extend to the plate boundary (Kluesner et al., 2013; Park et al., 2002; Watson et al., 2020), and as such, are potential sites of fluid discharge from within the wedge and along the megathrust (Hensen et al., 2004; Martin et al., 1996; Mottl et al., 2004; Philip et al., 2023; Ranero et al., 2008; Tryon et al., 2010). Deeply-sourced fluids have compositions that are distinct from seawater as a result of diagenetic reactions that proceed with increasing temperature and pressure (Kastner et al., 2014). These reactions uniquely change the fluid composition, providing a signature that is often maintained during transport from depth to expulsion at seafloor seeps. In this way, concentrations of various solutes in seep fluids are indicative of the temperature/pressure regime from which the fluid was sourced, providing information on the region of the subduction zone that is actively draining. Further, numerical modeling of seep pore water solute profiles yields field-based fluid flow rate estimates that can be compared to margin-scale model predictions and can indicate the efficiency of fluid drainage along fault zones. Together, the source and expulsion rate of fault-hosted seep fluids serve as valuable indicators of the permeability of fault zones and pore fluid pressure at depth.

Here we present the results of a systematic and comprehensive field campaign that includes 90 heat flow measurements and sampling of pore fluids from 33 piston, gravity, and push cores spanning the deformation front to the upper slope at the southern and northern HSZ. We determine heat flow, fluid flow rates, and fluid compositions at seafloor seeps associated with faults to better understand the permeability architecture of the forearc and make inferences of the pore fluid pressure conditions in the region of shallow slow slip at the northern HSZ.

2. Methods

2.1. Sample Collection

During the 38-day SAFFRONZ (Slow-slip and Fluid Flow Response Offshore New Zealand) expedition on the *R/V Revelle* in early 2019 (RR1901/RR1902), we investigated 14 sites spanning from the deformation front to the upper slope offshore of the southern and northern Hikurangi margin (Figure 1). Site selection was guided by the known distribution of seepage indicators described in Watson et al. (2020). Hydroacoustic surveys for bubble plume detection, collection of 90 heat flow measurements, and seafloor surveys using the remotely operated vehicle (ROV) *Jason* during the 2019 expedition further refined our coring locations. We specifically targeted fault-hosted sites of fluid emission, that is, seafloor seeps located at the up-dip projections of fault zones or on seafloor ridges marking the hanging-walls of thrust systems (Figure 2). Two piston cores, 58 gravity cores, and 19 push cores were collected for pore water geochemistry.

Heat flow determinations were made using a "violin bow" style multipenetration heat flow probe at a nominal spacing of about 200 m near seep sites with the goal of locating areas of warm fluid discharge to guide coring and ROV operations. The probe's thermistor string is 3.5-m long and houses 11 thermistors. Once seep sites were targeted, additional heat flow determinations were made with either a 0.6-m or 1.0-m probe on the ROV *Jason*. The ROV probes house five thermistors and measurement spacing was generally less than ~10 m. Determinations

10.1029/2024GC011778

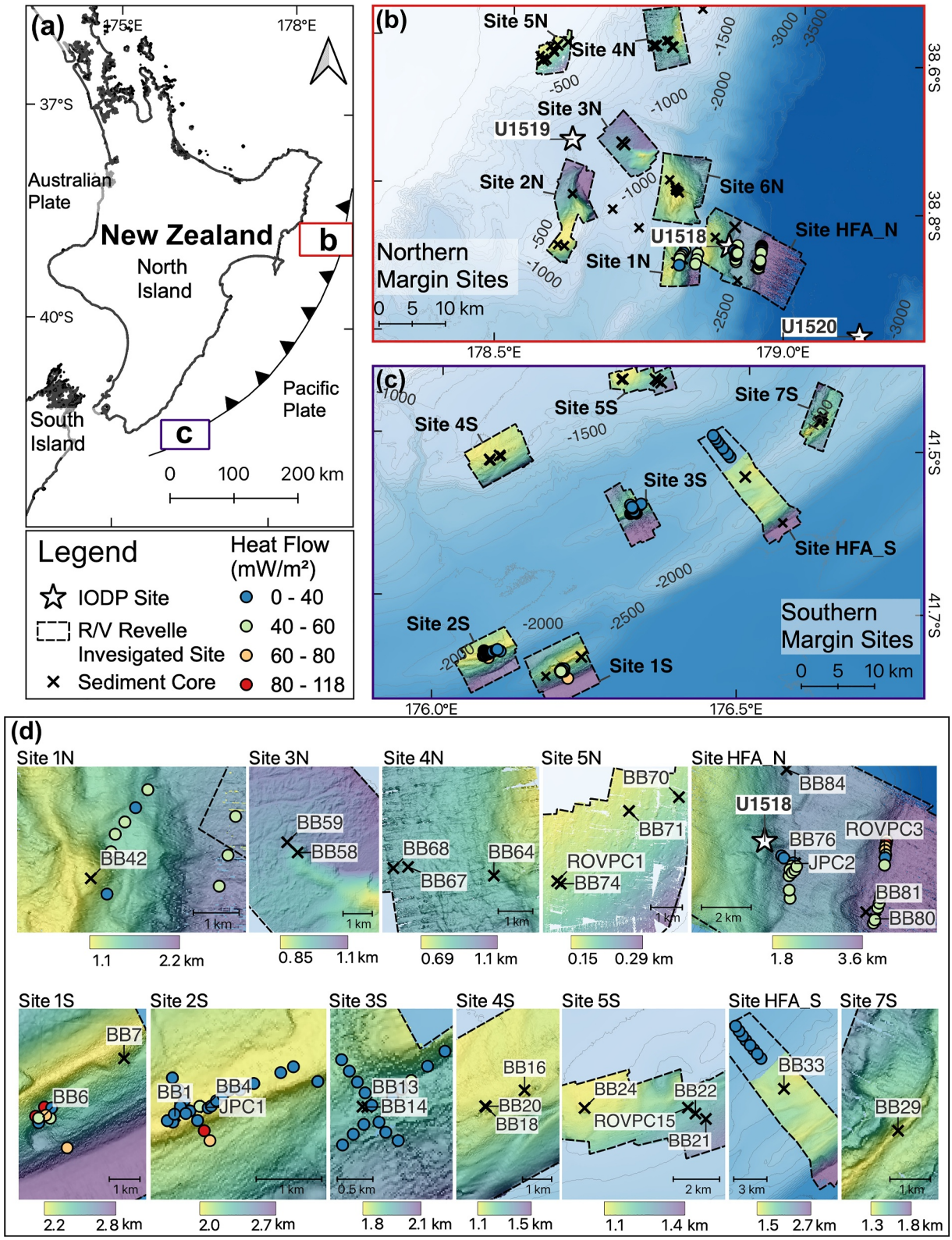

Figure 1. (a) Regional map of New Zealand's North Island. Black saw-toothed line shows deformation front. (b, c) Locations of all collected cores, heat flow measurements using 3.5-m probe, and International Ocean Discovery Program Sites U1518, U1519 and U1520. 500-m bathymetric contours are labeled. (d) Zoom-in of the sites, 33 cores, and 90 heat flow measurements that are the focus of this study. Color-bars show bathymetry (km).

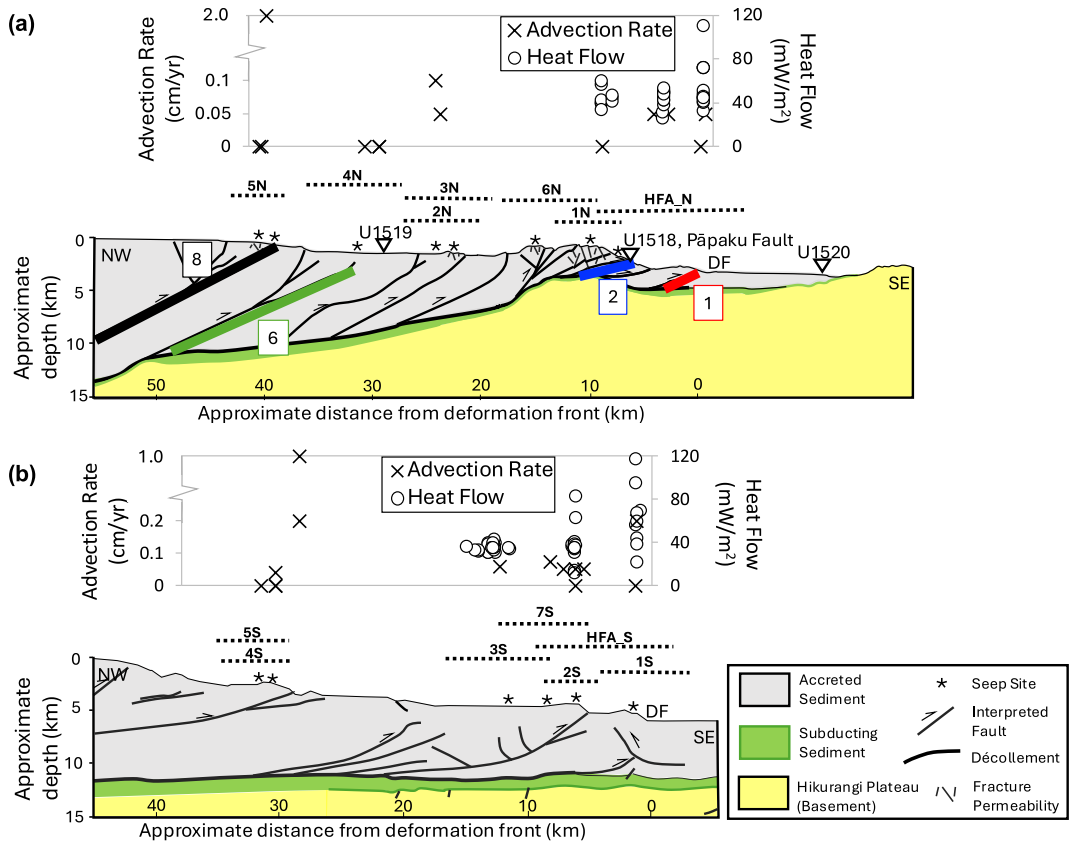

Figure 2. Conceptualized cross sections of (a) the northern Hikurangi margin, based on Watson et al. (2020) and (b) the southern Hikurangi margin, based on the interpretations of seismic line SAHKE-01 by Bland et al. (2015). Approximate locations of our study sites are projected onto the cross sections, indicated by the dotted lines. Plots of heat flow and pore water advection rate results are also projected onto the cross sections; Y-axes are "broken" to show the spread of low advection rates. Thick colored lines in panel (a) reflect the four fault geometries used in the diffusive loss modeling (Figure 6). International Ocean Discovery Program Sites U1518, U1519, and U1520 are shown as white triangles. Note site locations, depths, and distances from the deformation front (DF) are approximates.

of heat flow consist of in situ measurements of the thermal gradient and thermal conductivity. Thermal conductivity was measured at most but not all sites. Where thermal conductivity was not measured it was estimated from nearby sites. All heat flow data was processed using software that allows iterative determination of the local thermal gradient and heat flux, including a Monte Carlo assessment of uncertainties (Stein & Fisher, 2001; Villinger & Davis, 1987). In total, 118 heat flow measurements were attempted with the 3.5-m probe. Of these, 90 were successful. Failed measurements were due to the inability of the probe to penetrate sediments, often attributed to authigenic carbonates at the seafloor.

Piston, gravity, and push cores were collected for pore water geochemical analysis across 14 sites. Piston cores were collected at two sites, averaging 7 m of penetration. Trigger cores (gravity cores that trigger the release of the piston corer upon hitting the seafloor) were collected alongside piston cores to ensure undisturbed samples of the top meter of sediment at those locations. Gravity cores were collected at all 14 sites, averaging about 3 m of penetration for successful cores. 101 gravity coring attempts were made, 58 of which were successful. 19 push cores (average recovery length of 20 cm) were collected at 8 sites using the ROV *Jason*. After collection, gravity and piston cores were immediately cut into 10–50 cm sections, capped, and stored in a cold room until further processing. Within ~24 hr, sediment was extruded at a 5 cm resolution in the top 20 cm of each core, and coarser resolution in deeper sections. Push cores were either similarly extruded in small sections or pore water was extracted using Rhizon samplers. During the extrusion process, 3 mL of sediment was collected from select samples using a cut-off syringe and placed into vials for later analysis of porosity. Extruded sediment sections were then squeezed for pore water using Ti squeezers and hydraulic presses. Each sample was passed through a

0.2 μm syringe filter before being dispensed into bottles and preserved for a range of post-expedition chemical analyses.

2.2. Pore Water and Sediment Analyses

Pore water salinity was measured shipboard using an optical hand-held refractometer. Alkalinity measurements were also conducted shipboard by Gran titration with HCl. Based on the profiles of alkalinity with depth, 33 cores were selected as representatives of the sites to be further analyzed on shore. Selected cores include 2 piston cores (JPC01, JPC02), 1 trigger core (JPC01_TC), 3 push cores (prefix ROVPC), and 27 gravity cores (prefix BB). Figure 1 shows the locations of all collected cores with labels only for the 33 cores that are the focus of this study.

Porosity was measured at the University of Washington (UW) by weighing 3 mL sediment samples before and after drying in an oven for 24 hr at 80°C. Pore water chloride concentrations were analyzed by titration with silver nitrate at UW following the method in Gieskes et al. (1991). Cl measurements were calibrated daily by comparison with at least 4 repeat analyses of IAPSO standard seawater to a precision of approximately 0.3%; reported concentrations are based on duplicate measurements of each sample. Concentrations of major (Ca, Mg, K, Na, S) and minor (B, Li, Sr, Fe, Mn, Si) elements were measured at Oregon State University using a Spectro Arcos ICP-OES, with samples diluted at 1:100 and 1:25 with a 1% and 2% nitric acid solution, respectively. Dilutions of IAPSO were used as calibration standards for the major elements. In-house standards prepared from certified reference standards were used for calibration of the minor elements. Analytical precision of major element analyses was <3%. Precision of B, Li, Fe, and Mn were <5%, and precision of Sr and Si were ≤6%. Sulfate was measured at UW using a Perkin Elmer ICP-OES with IAPSO as the calibration standard. Sulfate analyses were only conducted for 6 sediment cores due to improper sample preservation; analytical precision was generally <5%. Ammonium was analyzed colorimetrically at UW following the method in Gieskes et al. (1991). Ammonium measurements were calibrated daily against a series of dilutions of an in-house solution prepared from certified ammonium chloride standard; analytical precision was <5% based on replicate analyses of a check standard. Analytical methods and results are included in (Aylward et al., 2024).

2.3. Reactive-Transport Modeling

We estimate in situ reaction rates and fluid advection rates using a one-dimensional finite-difference model that solves the transient advection-diffusion equation run to steady-state (Berg, 2018),

$$\phi \frac{\partial C}{\partial t} = \frac{\partial}{\partial z}\left[D_s \phi \frac{\partial C}{\partial z}\right] - \frac{\partial}{\partial z}\left[(\phi b + \phi v)\, C\right] \pm \phi R, \tag{1}$$

where C is solute concentration, t is time, z is depth, D_s is the sediment diffusion coefficient, ϕ is porosity, b is pore water burial rate, v is fluid advection rate, and R is the sum of the rates of in situ reactions.

Diffusion coefficients are calculated based on a reference diffusivity adjusted for temperature (T), salinity (S), and tortuosity $\left(\theta^2\right)$. We use the Stokes-Einstein relationship to calculate molecular diffusion coefficients,

$$D_m = \left(\frac{T}{\mu}\right)\left(\frac{\mu_r}{T_r}\right)(D_r), \tag{2}$$

where $\mu(T,S)$ is the fluid dynamic viscosity as a function of temperature and salinity, and μ_r is the viscosity at the reference temperature and salinity calculated following Sharqawy et al. (2010). D_r is the reference diffusion coefficient at the reference temperature, T_r (Li & Gregory, 1974). The sediment diffusion coefficient is then,

$$D_s = \left(\frac{D_m}{\theta^2}\right), \tag{3}$$

where sediment tortuosity is calculated from porosity (ϕ) as (Boudreau, 1997),

$$\theta^2 = 1 - ln\left(\phi^2\right). \tag{4}$$

We estimate advection rates by modeling NH_4 profiles. Ammonium concentrations increase within our cored depth range and do not reach an asymptotic value, so we use NH_4 profiles from International Ocean Discovery Program (IODP) Sites U1518 and U1519 (locations shown in Figures 1b and 2a) to represent background, non-seep conditions without fluid advection ($v = 0$). At these sites, we estimate zoned NH_4 reaction rates (R in Equation 1) with depth from the seafloor ($NH_4 = 0$ μM) through the upper sediments. Model input parameters (Table S1 in Supporting Information S1) include NH_4 concentrations, porosity, and temperature gradients at U1518 and U1519 from Wallace et al. (2019) and sedimentation rates from Crundwell and Woodhouse (2022). Fixing the reaction rate profiles, we can then model NH_4 profiles at a range of advection rates. Advection rates for our cores are then estimated by finding the best fit between our measured pore water NH_4 profiles with the advection models generated at the drilling sites. For both the northern and southern margin, Site U1519 is used as the reference site for cores taken on the mid- to upper-slope, and U1518 as the reference site for cores taken closer to the deformation front. This modeling assumes the U1518 and U1519 NH_4 profiles are representative of the bottom boundary concentrations and that in situ NH_4 reaction rates at the reference locations are applicable to the shallow section of seep sediments.

In addition, we estimate the solute concentration change due to diffusion during fluid transport along faults by sequentially implementing the two-dimensional model of Vasseur et al. (1993). We first solve for temperature to compute the sediment diffusion coefficient and then solve for solute concentration. The model consists of a thin, permeable, and dipping fault that traverses a homogenous impermeable medium with a specified flow rate. Fluid is assumed to enter the base of the fault at the ambient temperature given by,

$$T = \Gamma z + T_0, \tag{5}$$

where Γ is the undisturbed thermal gradient, z is depth, and T_0 is the bottom water temperature. This fluid then flows upward along the fault at a specified flow rate (q), moving heat from the downdip portion of the fault and warming the updip portion of the fault. The temperature disturbance (ΔT) due to fluid flow along the fault is (Vasseur et al., 1993),

$$\Delta T(x) = \frac{Pe\,\Gamma\tan(\varphi)}{1 - Pe\tan(\varphi)}\left[h(x) - h_0\left(\frac{h_0}{h(x)}\right)^{\frac{1}{Pe\,\tan(\varphi)}}\right], \tag{6}$$

where x is the horizontal distance, h_0 is the depth to the base of the fault at $x = 0$, $h(x)$ is the along-fault depth, φ is the fault dip, and Pe is the Peclet number. The Peclet number is the ratio of the advective and diffusive flow rates,

$$Pe = \frac{q\,\rho_f c_f}{\lambda}, \tag{7}$$

where q is the flow rate, λ is thermal conductivity, and ρ_f and c_f are the fluid density and specific heat, respectively, calculated as a function of pressure and temperature (Nayar et al., 2016; Sharqawy et al., 2010). The background temperature field is given by,

$$\frac{1}{\alpha}\left(\frac{\partial^2 T}{\partial x^2} + \frac{\partial^2 T}{\partial z^2}\right) = 0, \tag{8}$$

where α is the thermal diffusivity, and x and z are the horizontal and depth dimensions, respectively. The sides of the model are held constant at the ambient temperature (Equation 5). Temperature along the fault is then given by,

$$T_{\text{fault}} = T + \Delta T, \tag{9}$$

and Equation 8 is solved by substituting T_{fault} for grid nodes along the fault.

With temperatures in hand, the sediment diffusion coefficient (Eqn. 3) is known. We repeat the procedure, solving Equation 6 for solute concentration disturbance (ΔC) instead of ΔT, replacing $Pe = \frac{qz}{D_s}$, and solving Equation 8

by replacing α with D_s and T with C, the solute concentration. The background concentration gradient between the surface and the base of the fault is given by,

$$\Gamma_c = \frac{C_{\text{base}} - C_0}{z}, \tag{10}$$

Where C_{base} is the solute concentration at the base of the fault, C_0 is the bottom water solute concentration, and z is depth. The sides of the model are set to $C = \Gamma_c z + C_0$.

3. Results and Discussion

3.1. Heat Flow

ROV determinations of heat flow show significantly higher values than those determined from the 3.5-m probe, but these high values appear to be associated with recent bottom water temperature variations. Because the ROV probes are relatively short, compared to the multipenetration probe, they are more susceptible to perturbations from recent bottom water temperature variations. Differences in mean heat flow values between the 3.5-m probe (mean value of 44 mW m^{-2}) and 0.6-m probe (mean value of 238 mW m^{-2}) are consistent with a change in bottom water temperature of about 0.3°C over a couple of weeks prior to our measurements. Although no long-term records of bottom water temperature exist at our study sites, temperature changes of this magnitude were observed during the 2014–2015 Hikurangi Ocean Bottom Investigation of Tremor and Slow Slip (HOBITSS) seafloor geodesy campaign (Wallace et al., 2016) at a water depth of 2.4 km along the northern margin. These inferences lead us to believe the ROV probe measurements are not suitable for detecting upward fluid advection and we do not discuss them further.

The locations and results of successful heat flow determinations using the 3.5-m probe are shown in Figures 1 and 2. Complete heat flow transects using the 3.5-m probe are shown in Figures S1–S6 in Supporting Information S1. The mean and standard deviation for these heat flow measurements are 44 and 17 mW m^{-2}, respectively. Sites 1N and HFA_N (Figures S1 and S2 in Supporting Information S1) targeted splay faults near the toe of the forearc in the northern margin. Heat flow results at these sites are generally low and inconsistent with warm fluid discharge, but a relatively high heat flow value was determined at Site HFA_N near kilometer 4 of the eastern profile (Figure S2 in Supporting Information S1). However, no seep is associated with this site; 3 ROV seafloor surveys and 6 cores during the 2019 expedition, as well as a subsequent deployment of a fluid flow meter (Aylward et al., 2023) do not reveal active seepage at site HFA_N. A possible explanation for this single anomalous value is slumping associated with deformation of the margin at this steeply sloped site, but without additional information, it is difficult to explain this single high value. Sites 1S, 2S, and 3S (Figures S3–S5 in Supporting Information S1) targeted seep sites along the southern margin. At Site 1S along profile A-A′ heat flow values between kilometer 0.4 and 0.7 are slightly higher than average (Figure S3 in Supporting Information S1) and near kilometer 0.4 of profile B-B′ a value >100 mW m^{-2} is observed. At Site 2S, values of ∼80 and 65 mW m^{-2} between kilometer 1.1 and 1.4 along profile A-A′ are observed (Figure S4 in Supporting Information S1). These high values are broadly consistent with upward fluid flow. Relatively low values of heat flow are also associated with Site 2S (Figure S4 in Supporting Information S1). One of these values is along transect A-A′ near kilometer 1 and the other along transect B-B′ near kilometer 0.75. These low values may be associated with recharging of fluids due to shallow gas emissions and bubble irrigation associated with the seep sites (e.g., Solomon et al., 2008).

3.2. Constraints on Fluid Sources From Pore Fluid Chemical Profiles

Select pore water solute profiles are shown in Figure 3; all pore water data are shown in Figures S7 and S8 in Supporting Information S1. Evident pore water deviations from seawater composition include increasing alkalinity, Si, Ba, and NH_4, and decreasing Ca, Li, and S concentrations with depth. Other solutes (K, Mg, Cl, Na, B, Sr) show near-vertical profiles that remain close to seawater concentrations. The most notable observation derived from this data set is that Cl concentrations (Figures 3a and 3f) do not show a significant negative deviation from seawater that would indicate freshening due to mineral dehydration, as has been widely documented at other margins (e.g., Brown et al., 2001; Hensen et al., 2004; Philip et al., 2023; Torres et al., 2004). The near-vertical Cl profiles suggest that the sampled seeps are not draining sediments that have undergone dehydration reactions, and

10.1029/2024GC011778

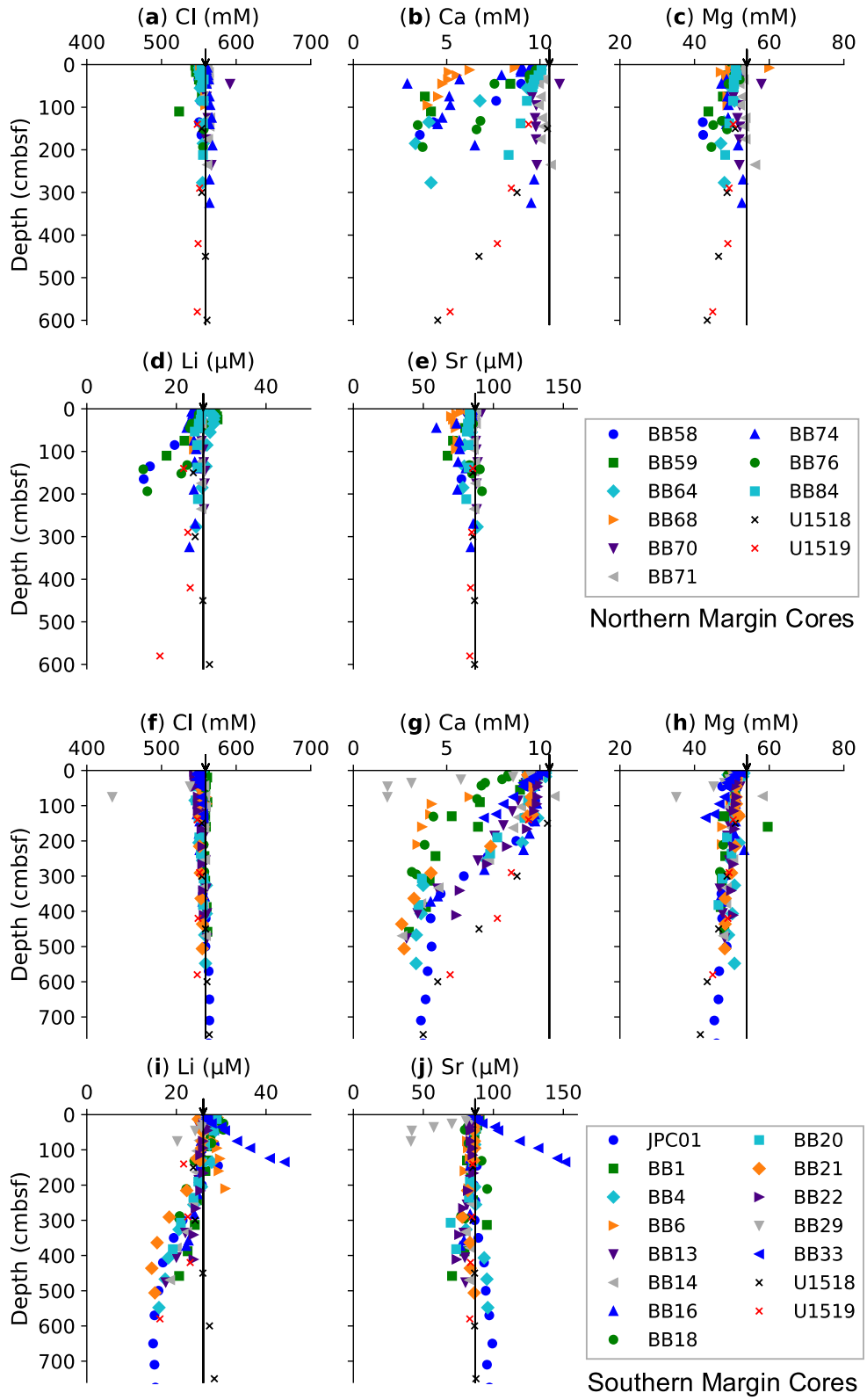

Figure 3. Select pore water solute profiles from gravity and piston cores taken at the northern (a–e) and southern (f–j) margin, along with the upper ~600–700 cm of pore water data from International Ocean Discovery Program Sites U1518 and U1519 (Wallace et al., 2019). Seawater concentration is denoted by a black arrow and vertical line.

thus are sourced from shallow depths. In the remainder of this section, we evaluate this inference in the context of additional geochemical and thermal data from the region.

The incoming sediment section at the northern HSZ was drilled at IODP Site U1520 (Wallace et al., 2019; location shown in Figures 1 and 2). Coring of the upper ∼510 mbsf recovered mainly trench-wedge facies and submarine slide materials (Barnes et al., 2020; Wallace et al., 2019; Figure S9 in Supporting Information S1). Below 650 mbsf, Site U1520 is thought to sample the protolith material for the plate interface, that is, the incoming plate interval that correlates to the plate interface zone (Barnes et al., 2020; Dutilleul et al., 2020). This protolith interval is composed largely of pelagic carbonates with alternating clay-rich layers (Lithologic Unit IV) and a highly altered volcaniclastic conglomerate with a smectite-based matrix (Lithologic Unit V) (Barnes et al., 2020; Wallace et al., 2019; Figure S9 in Supporting Information S1). Analysis of these units suggests low to moderate bound water content in the Unit IV marls (∼2%–15%) and chalks (∼2%), and very high hydrous mineral content (up to ∼22%) in the Unit V smectite-rich volcaniclastic conglomerates (Dutilleul et al., 2020). The smectite to illite transition reaches peak fluid production at 60–150°C, producing fluid in proportion to the amount of smectite present. Thermal modeling of the northern HSZ predicts that temperatures reach this range along the plate boundary between 10 and 50 km landward of the deformation front (Antriasian et al., 2019; Figure S10 in Supporting Information S1). Thus, if fluids originating from within or below the plate interface 10–50 km landward of the deformation front are discharging at seep sites, they should carry low chloride concentrations indicative of smectite (and zeolite) dehydration reactions in the volcaniclastics (Lithologic Unit V).

The fault-hosted seep sites we sampled in the northern margin span the area from the deformation front to the shelf break approximately 40–45 km landward (Figure 2); these sites overlap the region of expected dehydration reactions (Figure S10 in Supporting Information S1). However, Cl concentrations in our sediment cores remain near seawater values, with end member concentrations generally ranging from 551 to 560 mM (Figure 3a). Despite sampling seep sites that are thought to tap deeper fluid sources, the near-seawater Cl concentrations indicate that these fluids likely originate from sediment compaction within the accretionary wedge, rather than dehydration of the lower wedge or underlying underthrust sediment. We are confident that the lack of low-Cl signal is not a mere product of dilution with seawater-Cl fluids from compaction sources given that modeling by Ellis et al. (2015) predicted the volumetric fluid release from smectite-illite transformation in the wedge (1.2 $m^3\ yr^{-1}\ m^{-1}$) and subducting sediments (1.8 $m^3\ yr^{-1}\ m^{-1}$) is ∼10% of the total fluid release from porosity change and mineral dehydration (∼30 $m^3\ yr^{-1}\ m^{-1}$), well within detectability of our methods. Further, these results are consistent with findings at IODP Site U1518: although Site U1518 sampled the westward-dipping Pāpaku thrust fault that extends from the megathrust to the seafloor at a depth of 304–322 mbsf, no low Cl signature was detected (Morgan et al., 2022; Wallace et al., 2019; Figure S9 in Supporting Information S1).

To test our interpretation of shallow fluid sources, we consider additional pore water geochemistry data from the incoming section drilled at Site U1520 (Figure S9 in Supporting Information S1). Pore fluid data from the lower section of subduction inputs (Lithologic Units IV and V) exhibit anomalous values of Sr, Mg, and Ca, that are easily distinguished from shallower accreted materials (Lithologic Units I–III) (Wallace et al., 2019; Figure 4 and S9 in Supporting Information S1). These signatures of the deeper units have been attributed to carbonate recrystallization toward dolomite (Wallace et al., 2019), which consumes Mg and releases Ca and Sr. In addition, a dissolved Li peak is observed at the transition between the shallower Unit III trench-wedge facies and deeper Unit IV pelagics, which has been interpreted to result from ash alteration (Luo et al., 2024). These anomalous signatures (low Mg, high Sr, Ca, Li) should be detectable in our samples if fluids were traveling from the plate boundary and deep wedge to the seafloor seeps.

Figure 4 shows the end member pore water concentrations of Li, Sr, Mg, and Ca for Lithologic Units I–V at Site U1520 (incoming sediments) and of the Pāpaku fault (U1518), alongside the end member composition from our seep cores in the northern margin. Pore water data of seep cores roughly fall on a mixing line connecting seawater values with the compositions of fluids from the shallowest sediments (Units I and II) from Site U1520 (Figure 4), indicating that the fluid chemistry is likely the result of mixing between those two sources. Mixing lines connecting seawater values with end member compositions of the deeper pelagics and volcaniclastics (Units IV and V) show how pore water composition would change for a given contribution of deeply sourced fluid. These scenarios demonstrate that even a small fraction of fluids from the plate boundary or deep wedge (e.g., 10%) would cause a noticeable shift in composition. Such a shift is not observed in any of our northern margin cores, nor are they observed in fluids sampled directly from the Pāpaku fault at IODP Site U1518.

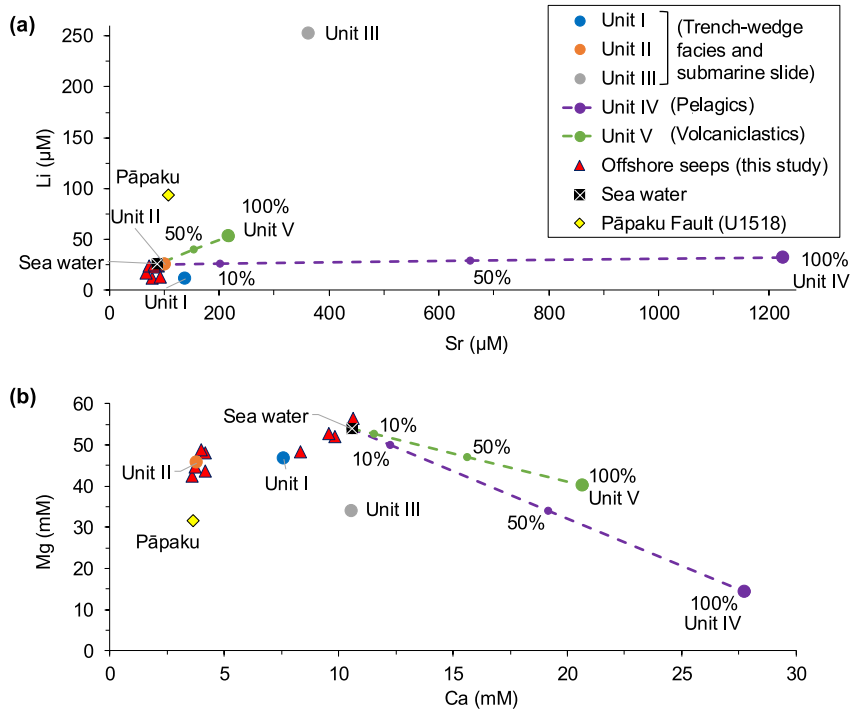

Figure 4. Cross plots of Li versus Sr (a) and Mg versus Ca (b) concentrations. Data points include end member concentrations for International Ocean Discovery Program (IODP) Site U1520 Lithologic Units I–V (Wallace et al., 2019), measurements from the Pāpaku fault at IODP Site U1518, and cores from the northern margin in this study. Dashed lines represent concentrations resulting from mixing seawater with U1520 pelagic carbonates (Unit IV) and volcaniclastics (Unit V).

Because the IODP drilling transect (Wallace et al., 2019) and thermal modeling (Antriasian et al., 2019) are confined to northern Hikurangi, we do not include our southern margin results on the cross plot comparisons with Site U1520 (Figure 4). The compositions of the southern margin cores, however, are generally comparable to those in the north, with no evidence of considerable alteration or input from mineral-dehydration reactions (Figures 3 and S7 in Supporting Information S1). However, two cores from the southern margin deviate from the norm. BB29 collected at Site 7S presents lower solute concentrations than average, explained by in situ carbonate mineral precipitation and gas hydrate dissociation upon core recovery. Numerous carbonate nodules and evidence of gas hydrate noted during shipboard processing of BB29 support this interpretation. Core BB33 taken at Site HFA_S, shows enrichment in Li and Sr not seen elsewhere. While these characteristics could signal fluid migration from depth, the enriched K and near-seawater Cl, S, B, and alkalinity also observed in this core are not consistent with enhanced fluid flow or deep sources. No known seep is associated with this site and heat flow determinations are not elevated. Instead, the enhanced Li and Sr in BB33 could be explained by ash dissolution/alteration which has been previously documented to release Sr and Li into the pore water at Hikurangi (Luo et al., 2023, 2024; Wallace et al., 2019). Overall, no systematic differences in geochemical observations between the northern and southern sites are observed despite the varying subducted sediment thicknesses and tectonic characteristics along the margin (e.g., incoming plate roughness, convergence rate, slip behavior).

In summary, the geochemistry results from sediment cores collected at fault-hosted seep sites in both the northern and southern margin lack evidence of deep-sourced fluid input or long-range fluid flow. Most notably, Cl concentrations show no contribution from dehydration reactions, and Sr, Mg, Ca, and Li concentrations do not reflect those observed in the deep incoming sediments sampled at U1520 (Figures 3 and 4). Moderate B and K values (Figures S7 and S8 in Supporting Information S1) also suggest shallow sediment-water reaction sources given that input from altered, higher-temperature fluid sources would cause a significant increase in B and reduction in K (Kastner et al., 2014; Philip et al., 2023) not observed in our cores. The fault-hosted seep fluids lack evidence for drainage of the plate boundary and instead suggest a shallow wedge-compaction source at temperatures lower than 60°C.

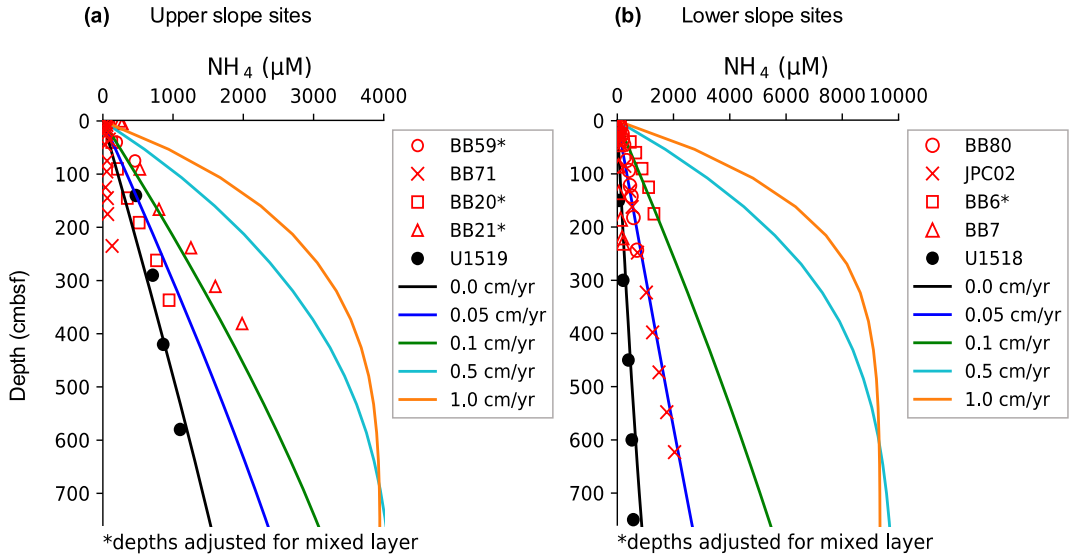

Figure 5. Select pore water solute profiles and advection model results. Measured pore water ammonium profiles for 8 example cores (red symbols), and for the upper ~700 cm at International Ocean Discovery Program Sites U1518 and U1519 (black circles). Solid lines show modeled ammonium profiles for Sites U1518 and U1519 given a range of upward advection rate scenarios. Cores located on the mid-upper slope of the northern and southern margin (Sites 3N, 4N, 5N, 4S, 5S in this study) are referenced to U1519 (a) and cores on the lower slope (Sites HFA_N, 1N, 1S, 2S, 3S, 7S, HFA_S in this study) are referenced to U1518 (b). We estimate the following upward advection rates (cm/yr) for the example cores based on best fit (by-eye) to modeled profiles: BB21–0.2; BB6, BB59–0.1; BB80, JPC02–0.05; BB20–0.04; BB7, BB71–0.

3.3. Modeled Fluid Flow Rates and Inferences on Fault Zone Permeability

Fluid advection rates at seep sites are estimated by best fitting the measured NH_4 data from our sediment cores to modeled advection rate scenarios at reference Sites U1518 and U1519. NH_4 profiles for eight cores (four northern margin and four southern margin cores) are plotted along with the model-generated advection rate scenarios in Figure 5, where positive values indicate upward fluid flow. Estimated maximum rates for all modeled cores are summarized in Figure 2 and Table S2 in Supporting Information S1. We note that cores with a mixed layer (vertical pore water solute profiles at seawater concentrations in the upper sediment column) are plotted from the base of the mixed layer to depth when estimating advection rates (e.g., BB6, BB59, BB20, and BB21 in Figure 5), where the depth of the mixed layer is based on the alkalinity profiles. Cores without a mixed layer (i.e., pore water solute profiles exhibit immediate excursions from seawater concentrations) are plotted from the seafloor to estimate advection rates (e.g., BB80 and JPC02 in Figure 5). Cores whose full NH_4 profiles remain near-vertical or are concave-up are plotted from the seafloor and listed as zero upward flow (e.g., BB7 and BB71 in Figure 5).

The rate of upward fluid flow varies between sites, ranging from ~0.04 to ~2 cm/yr. Similar to the pore fluid composition, the observed variations do not show a systematic or predictable change from north to south along strike, or from trenchward to landward across strike (Figure 2, Table S2 in Supporting Information S1). In the northern margin, the highest estimated flow rate for piston and gravity cores is ~0.1 cm/yr upward (BB59) located about 22 km landward of the deformation front. The remaining piston and gravity cores have rate estimates of <0.1 cm/yr upward. Estimated rates from southern margin piston and gravity cores are similarly low, with maximum rates of ~0.2 cm/yr upward (BB21). Two push cores, ROVPC1_1121 (northern margin) and ROVPC15_1115 (southern margin) give the highest flow rates estimates of ~2 and ~1 cm/yr, respectively. Notably, even the cores with the highest upward flow rates (e.g., ROVPC15_1115 and BB21) do not show geochemical signatures of deeply-sourced fluids (i.e., low Cl, K, high B, Li, Sr).

The range of modeled fluid flow rates is relatively low (generally ≤0.2 cm/yr) despite targeting seeps associated with fault zones that could channel fluid flow. We compare our estimated rates to the seafloor seepage rate predictions at fault zones in the outer forearc of subduction zones by Sun et al. (2020a). They use a numerical modeling approach in which mechanical loading, deformation, and fluid drainage are fully coupled. Given fault zone permeabilities that are considerably enhanced relative to sediment matrix permeabilities (Sun et al., 2020a,

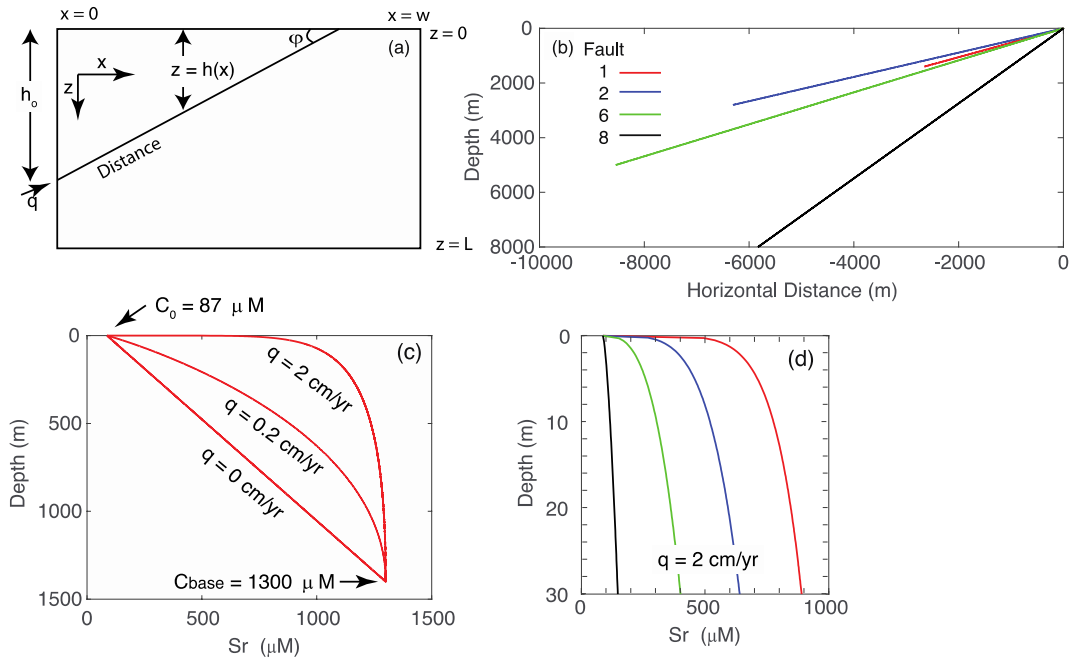

Figure 6. Model of geochemical signal attenuation due to diffusive loss along a flow path. (a) Geometry of 2-D fault model with fluid flow rate q (cm/yr). (b) Schematic for four fault geometries tested. (c) Sr concentration along Fault 1 given three different flow rates. (d) Sr concentration along faults near the seafloor for q = 2 cm/yr. Color scheme for (b, d) is same as that shown in Figure 2.

models REF, MK2, FK2), their models predict seafloor seepage rates of 10 cm/yr at fault zone locations. Our estimated flow rates are more compatible with model scenarios of little to no fault zone permeability enhancement, which predict rates of <5 cm/yr (Sun et al., 2020a models FK1, FK3). In summary, sediment cores from both the northern and southern Hikurangi margin provide geochemical evidence for low fluid flow rates that do not vary systematically, and imply relatively low fault zone permeability.

3.4. Attenuation of Geochemical Signals Due To Diffusive Loss Along Flow Path

Given the low fluid flow rates we estimate at fault-hosted seeps (≤2 cm/yr), we consider whether the lack of a geochemical signal of underthrust fluids (i.e., anomalous solute concentrations) could be due to diffusional loss during fluid migration from depth (e.g., Saffer & Screaton, 2003). To test the expected solute concentration loss due to diffusion to the surrounding sediment matrix during fluid transport along faults, we apply the diffusional loss model (Equations 5–10) to four representative fault geometries (Figures 2 and 6, Table 1). Fault length, depth of fault at $x = 0$ (h_0), and fault dip (φ) span the range of splay fault geometries along seismic line 05CM-04 at the northern Hikurangi margin (Barker et al., 2018). We calculate temperature at the bottom boundary (T_{base}) from the bottom water temperature (T_0) and the thermal gradient (Γ), based on results from Antriasian et al. (2019). Thermal conductivity ($\lambda = 0.9$ W/m K) is based on measurements from Antriasian et al. (2019) and we use a

Table 1
Fault Parameters for Diffusional Loss Model

Fault	Fault length (km)	h_0 (km)	φ (°)	T_0 (°C)	T_{base} (°C)	Γ (°C/km)	ϕ	C_0 (μM)	C_{base} (μM)
1	3	1.4	28	2	20	13	0.35	87	1,300
2	6.9	2.8	24	2	30	10	0.25	87	1,300
6	9.9	5	30	2	50	10	0.2	87	1,300
8	9.9	8	54	2	150	18	0.1	87	1,300

Note. h_0–depth of fault at $x = 0$; φ–fault dip; T_0–temperature at $z = 0$; T_{base}–temperature at $x = 0$; Γ–undisturbed thermal gradient; ϕ–porosity; C_0–Sr concentration at $z = 0$; C_{base}–Sr concentration at $x = 0$.

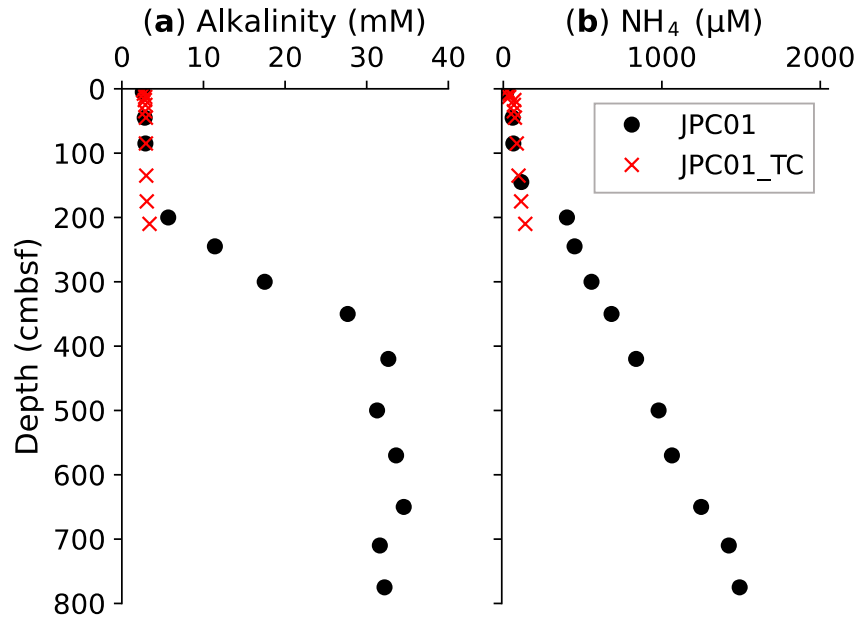

Figure 7. Pore water alkalinity (a) and ammonium (b) for piston core JPC01 and associated trigger core JPC01_TC. The trigger core did not penetrate deep enough to capture the advective signal observed in the piston core.

thermal diffusivity (α) of 1×10^{-6} m^2/s. Porosity (ϕ) is based on model results from Ellis et al. (2015). We use Sr as the modeled solute because the high Sr concentrations measured in the pelagic section of the incoming sediments at Site U1520 (Lithologic Unit IV) serve as an effective tracer of deep fluids. The Sr concentration at the seafloor (C_0) is the seawater value (Table 1), and the Sr concentration of 1,300 μM at the bottom boundary (C_{base}) is the maximum Sr measured in the pelagic sediments at U1520 (Figure S9 in Supporting Information S1). We note that the bottom boundary of 1,300 μM Sr is a minimum value, as carbonate recrystallization will continue to add Sr to the pore water during subduction. We test fluid flow rates (q) that span order of magnitude estimates from our observations (0.2–2 cm/yr).

Using an along-fault fluid flow rate of 2 cm/yr, we find that complete diffusive loss of the high Sr signal does not occur in any of our four tested fault lengths (Figure 6d). Only in modeling the longest, steepest-dipping tested fault (Fault 8, 9.9 km long) does the model predict considerable attenuation of the signal such that expected concentrations fall near the point of detectability of our methods. Testing a lower advection rate of 0.2 cm/yr predicts greater signal attenuation, but enhanced Sr concentrations are still detectable along Faults 1 and 2 near the deformation front (Fault 1 shown in Figure 6c). The resulting persistent high Sr concentrations for representative Faults 1, 2, and 6 at an advection rate of 2 cm/yr, and Faults 1 and 2 at 0.2 cm/yr (Figure 6) discount the hypothesis that diffusional loss alone causes the lack of deeply-sourced fluid signals in our seep samples or the lack of a signal along the Pāpaku Fault drilled at IODP Site U1518 (Wallace et al., 2019).

3.5. Gas-Driven Processes Generate Mixed Layers in Shallow Sediments

When discussing our approach for modeling advection rates using NH_4 profiles, we noted that some of the cores collected at seep sites show near constant solute concentrations in the uppermost sediment, followed by the concave-down profiles below that are indicative of upward fluid advection beneath a mixed layer. For example, JPC01 (Figures 3 and 7 and S7 in Supporting Information S1), collected from a seep site in the southern margin, shows concave-down profiles of Ca, S, Li, alkalinity, SO_4, and NH_4 beneath vertical profile segments at seawater concentrations that extend ~145 cmbsf. Overprinting the geochemical effects of in situ reactions and upward fluid advection, the vertical profiles in the upper sediments reflect rapid sea water irrigation. The thickness of the mixed layer observed at our seepage locations generally ranges from 4 to 235 cm (Table S2 in Supporting Information S1). As a result, cores with shallow penetration (≤~200 cmbsf) often have near-vertical profiles with depth (e.g., JPC01_TC, Figure 7) despite close proximity to seepage indicators because they do not penetrate deep enough to surpass the mixed layer.

The kinked pore water profile shapes we observe in many seep cores (near-seawater solute concentrations in upper pore fluids and concave-down profiles below) indicate that the rate of seawater irrigation in the upper 10s of centimeters is greater than the rate of upward advection from depth. This phenomenon is ubiquitous at seep sites globally. Observations of mixing in the upper ∼1 m sediment are documented, among others, in the Gulf of Mexico (e.g., Solomon et al., 2008), the Sea of Okhotsk (e.g., Haeckel et al., 2007), and in the Cascadia (e.g., Tryon et al., 1999), Svalbard (Hong et al., 2016), and Barbados (Henry et al., 1996) margins. Mixing of bottom water into the uppermost part of the sediment column has been attributed to bio-irrigation (e.g., Aller, 1982), recent, rapid emplacement of sediments (e.g., mass transport deposits; Hensen et al., 2003; Hong et al., 2014), bubble irrigation (Haeckel et al., 2007), and gas-driven aqueous pumping (Solomon et al., 2008; Tryon et al., 1999). While a quantitative assessment of the rate and impact of such mixing is beyond the scope of this paper, it is likely important for the flux of many solutes across the sediment water interface at seeps worldwide, particularly those that are most impacted by early diagenetic reactions such as SO_4, Ca, Mg, and alkalinity.

3.6. Implications for Pore Pressure Accumulation and the Occurrence of Slow Slip

Fluids are sourced at depth along the Hikurangi margin through both sediment compaction and mineral dehydration. As observed at other subduction zones (e.g., Hensen et al., 2004; Martin et al., 1996; Philip et al., 2023; Ranero et al., 2008; Torres et al., 2004), we expected to see evidence of these fluids rapidly expelled at structurally controlled seep sites, which are thought to serve as efficient flow paths from depth. We sampled sites of known fluid emission in the northern and southern margin and do not observe evidence of plate boundary drainage from any fault zone. There is no geochemical evidence of deeply sourced fluids at our coring locations or along the Pāpaku Fault drilled at IODP Site U1518. Furthermore, the shallowly sourced fluids we sampled are expelled at low rates (up to 2 cm/yr but generally ≤0.2 cm/yr), compatible with model scenarios of little to no fault zone permeability enhancement (Sun et al., 2020a). These observations imply that fluids along the plate boundary and in surrounding sediments (a) are draining laterally and exiting at as-yet unsampled seep sites seaward of the deformation front; (b) have limited vertical drainage and are accumulating in the wedge; or (3) are trapped at depth, causing high pore pressures along the plate boundary.

Lateral flow could occur along permeable sediment layers (e.g., the turbidites of Lithologic Unit III drilled at Site U1520) after vertical flow into the wedge, or possibly through the fractured basalts of the incoming plate and subducting seamounts, which are likely more permeable than surrounding sediments (e.g., Solomon et al., 2009). If significant lateral drainage of fluid is occurring, the sites of fluid expulsion at the seafloor have not yet been sampled. Given the extent of our sampling program, which targeted all known seep sites identified during several surveys of the region (Watson et al., 2020), we argue that this scenario is unlikely landward of the deformation front. We cannot discount long-distance lateral drainage and fluid expulsion farther seaward. However, the longer flow pathways would not be as efficient as focused flow along splay faults and thus would not be as effective at regulating pore fluid pressure.

In scenario two, deeply sourced fluids may be draining from the plate boundary, possibly aided by damage associated with seamount subduction in the northern margin (Chesley at el., 2021; Sun et al., 2020b), and stored within the overlying wedge. Fluid storage following drainage into the wedge is consistent with electromagnetic observations that identify regions of anomalous porosities in the lower wedge (Chesley et al., 2021), and seismic observations that identify areas of overpressure in portions of the wedge (e.g., Arnulf et al., 2021). This option is perhaps most compatible with drainage of the plate boundary and underthrust sediments via fault-valving (Sibson, 1990). In the fault-valve model, fluid pressures are cyclically accumulated and then released with fault slip that temporarily opens fluid migration pathways. This model is supported by several lines of geophysical evidence at northern Hikurangi, including the evolution of earthquake focal mechanisms (Warren-Smith et al., 2019), Vp/Vs and shear wave splitting delay times (Zal et al., 2020), and repeating earthquakes (Shaddox & Schwartz, 2019). However, transient fluid pulses from depth during this process would generate visible geochemical signals in our data set if fault zones acted as efficient vertical pathways for fluid transport to the seafloor. As shown in other regions where fluid discharge is episodic, the pore water profiles will show non-steady state characteristics that can last on the order of thousands of years (Hong et al., 2016). We postulate that trapping of fluids within the wedge could explain the lack of geochemical evidence for a previous discharge pulse despite geophysical inferences for fault-valving at northern Hikurangi.

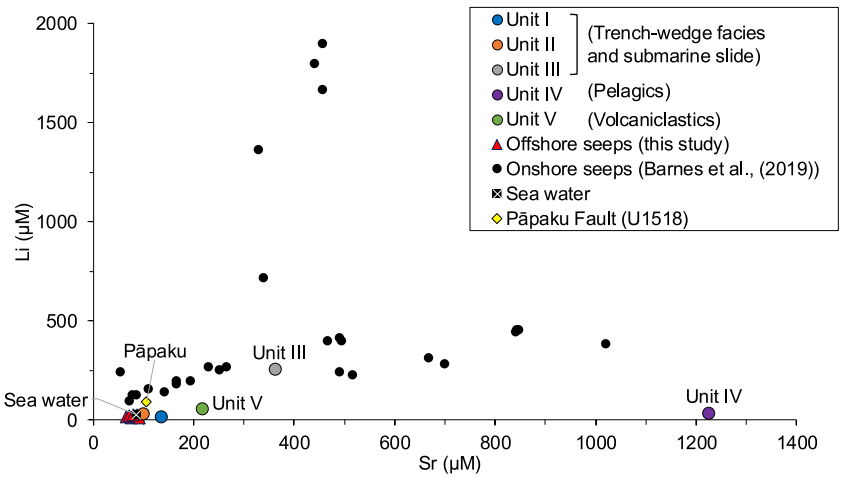

Figure 8. Cross plot of Li versus Sr concentrations at onshore seeps sampled in the northern margin (Barnes et al., 2019), endmember concentrations of International Ocean Discovery Program (IODP) Site U1520 Lithologic Units I–V, the Pāpaku fault at IODP site U1518, and cores from the northern margin in this study.

At the southern margin, early, efficient drainage of the subducting sediments into the upper plate in the region of our southern margin sites has been inferred from seismic data (Crutchley et al., 2020). However, while several anomalous heat flow values near the deformation front (Sites 1 and 2S; Figures 1, S3, and S4 in Supporting Information S1) may be indicative of local fluid advection, pore fluid compositions at the sampled seeps do not reflect deep fluid sources. Instead, our geochemical results indicate that fluids draining from the plate boundary and subducting sediments do not reach the seafloor. Thus, fluids may remain trapped in the outer wedge at this portion of the southern margin. This interpretation is compatible with the presence of a low seismic velocity zone at the base of the frontal thrust fault in the lower wedge beneath Site HFA_S, which has been interpreted as a zone of high pore fluid pressure resulting from compressional deformation and upward drainage of subducting sediments (Crutchley et al., 2020).

A third scenario to explain our observations is that in the absence of efficient drainage, fluid input from the compaction and dehydration of the smectite-rich volcaniclastics that make up the lower subduction inputs, would lead to overpressure along the plate boundary. This interpretation is consistent with geophysical studies that have imaged high-reflectivity zones (Bell et al., 2010), high conductivity/low resistivity anomalies (Heise et al., 2017), and low Vp and high Vp/Vs (Eberhart-Phillips & Bannister, 2015) at northern Hikurangi. These observations have been interpreted as fluid-rich, overpressured zones along and surrounding the plate interface in the region of slow slip. Numerical models that prescribe low splay fault and megathrust permeabilities are also in line with these interpretations, predicting high fluid pressures at depth and low fluid flow rates at the seafloor (Ellis et al., 2015; Sun et al., 2020a).

In summary, our results of shallowly sourced, slow-flowing fluids at fault-hosted seeps indicate that splay fault and megathrust permeabilities at the Hikurangi margin are low, leading to relatively poor vertical drainage of the lower-wedge, plate boundary, and underthrust sediments to the seafloor. This in turn may result in the development of an overpressured system that spans from the deformation front to the upper slope. Initial results from the NZ3D seismic reflection experiment at the northern margin imaged high-velocity layers at the base of the hanging wall of faults in the outer forearc (Gase et al., 2023; Han et al., 2022), interpreted as low-permeability carbonate layers which disrupt BSR (bottom simulating reflector) continuity and potentially inhibit fluid flow along fault planes (Han et al., 2022). These findings provide one possible explanation for low splay fault permeability and poor fluid drainage along fault zones offshore northern Hikurangi.

However, there is evidence of deeply sourced fluid venting landward of the upper slope region, at onshore seeps ~75 km landward of the deformation front. Previous studies that sampled onshore springs along the margin have reported signatures of deeply sourced fluids as well as a systematic decrease in solute concentrations from north to south (Barnes et al., 2019; Reyes et al., 2010). Figure 8 shows a cross plot of Li versus Sr concentrations which showcases the composition of the onshore seep fluids. Unlike the offshore seeps sampled in this study, onshore

forearc seeps (those plotted are from the northern margin only) exhibit highly altered fluid compositions with enhanced Li and Sr concentrations indicative of inputs from deep sources. Barnes et al. (2019) attributed variation in seep composition along strike to changes in upper plate structural permeability rather than a systematic change in fluid source along the margin.

The venting of fluids from deep sources at onshore seeps in the northern margin may be enabled by the transition from a compressional to extensional stress regime, which enhances upper-plate permeability (McNamara et al., 2021; Sibson & Rowland, 2003). A modeled enhancement in effective coefficient of friction at ~50 km landward of the deformation front based on heat flow measurements is consistent with the onset of extension in the upper plate marking the down-dip extent of overpressure along the plate boundary (Antriasian et al., 2019). The Tuaheni Seep Field (Site 5N in this study) on the shelf break at the northern margin, lies just seaward of this onset of extension. We did not sample deeply sourced fluids at this site, but the active, dense fluid expulsion recorded at this location (>1,700 seep indicators covering ~90 km^2; Watson et al., 2020) suggests enhanced permeability. A tectonically driven change in permeability structure likely explains the change from inefficient drainage of the plate boundary along faults in the offshore forearc to efficient drainage observed at onshore seeps, associated with the transition from compression to extension ~50 km landward of the deformation front.

4. Conclusions

We collected heat flow measurements and performed geochemical analyses on pore water of sediment cores taken at structurally controlled seep sites spanning the continental slope of the southern and northern Hikurangi margin. We do not observe evidence for wide-spread warm fluid discharge, or deeply sourced or dehydration-derived geochemical signals at our sample sites. Cl concentrations are at near seawater composition in all our cores even though the plate boundary is within the modeled temperature range for clay mineral dehydration. Additionally, near-seawater Li, B, and Sr concentrations in offshore seep fluids provide no evidence of contributions from the protolith material for the plate interface (the pelagic and volcaniclastic Units of the incoming section at IODP site U1520). Modeled upward fluid advection rates are relatively low, ranging from ~0.04 to 2 cm/yr. Overall, our results from offshore seeps show no evidence of appreciable drainage of the plate boundary along fault zones.

This result contrasts with observations at many other subduction zones of seep fluid geochemical signatures indicative of long-distance transport from plate boundary depths. Deep-sourced fluids have been identified at seeps along Barbados (Martin et al., 1996), Nankai (Pape et al., 2014; Toki et al., 2014), Costa Rica (Hensen et al., 2004; Ranero et al., 2008), Chile (Scholz et al., 2013), Marianas (Mottl et al., 2004), and Cascadia (Philip et al., 2023) using sediment cores with similar penetration depths to our samples. Instead, shallow fluid sources and low flow rates at Hikurangi suggest that fault zones from the deformation front to the upper slope are relatively impermeable at depth and prevent efficient drainage of the megathrust and surrounding sediments to the seafloor. Our results are consistent with a plate boundary and/or lower wedge that is poorly drained and overpressured, likely influencing the occurrence of slow slip.

Acknowledgments
This work is supported by NSF awards OCE-1753617 and OCE-1753665. MET acknowledges support from a fellowship by the Hanse-Wissenschaftskolleg Institute for Advanced Study (HWK), Germany. We thank the science party, captain and crew of the R/V *Revelle*, the Oregon State University coring facility (MARSSAM), and the ROV *Jason* team onboard during the 2019 expedition for making this work possible. Special thanks to Jess Hillman for assistance with onshore logistics and hydroacoustic surveys on the SAFFRONZ expedition, Valerie Stucker for providing laboratory space in New Zealand for cruise preparations, Brendan Philip for assistance with hydroacoustic surveys, and Theresa Whorley for assistance with pore water sampling. We are grateful to Gareth Crutchley and one anonymous reviewer whose thoughtful comments improved this manuscript.

Data Availability Statement

All pore water geochemistry data produced for this study are publicly available at https://doi.org/10.60520/IEDA/113176 (Aylward et al., 2024). Heat flow data are available at https://www.marine-geo.org/tools/files/31405 (Harris et al., 2023).

References

Aller, R. C. (1982). The effects of macrobenthos on chemical properties of marine sediment and overlying water. In *Animal-sediment relations: The biogenic alteration of sediments* (pp. 53–102). Springer US. https://doi.org/10.1007/978-1-4757-1317-6_2

Antriasian, A., Harris, R. N., Tréhu, A. M., Henrys, S. A., Phrampus, B. J., Lauer, R., et al. (2019). Thermal regime of the northern Hikurangi margin, New Zealand. *Geophysical Journal International*, *216*(2), 1177–1190. https://doi.org/10.1093/gji/ggy450

Arnulf, A. F., Biemiller, J., Lavier, L., Wallace, L. M., Bassett, D., Henrys, S., et al. (2021). Physical conditions and frictional properties in the source region of a slow-slip event. *Nature Geoscience*, *14*(5), 334–340. https://doi.org/10.1038/s41561-021-00741-0

Aylward, I., Solomon, E. A., Whorley, T. L., Miller, R., Hillman, J. I. T., Seabrook, S., et al. (2023). The evolution of fluid flow throughout the slow slip cycle: Testing the hydrologic response to SSEs at the Hikurangi subduction zone. Presented at AGU Fall Meeting 2023. San Francisco, CA.

Aylward, I. E., Solomon, E., Torres, M., Harris, R., & Whorley, T. (2024). Marine sediment porosity and pore water chemistry from the Hikurangi margin, offshore the North Island of New Zealand (Version 1.0) [Dataset]. *Interdisciplinary Earth Data Alliance (IEDA)*. https://doi.org/10.60520/IEDA/113176

Bangs, N. L., Morgan, J. K., Bell, R. E., Han, S., Arai, R., Kodaira, S., et al. (2023). Slow slip along the Hikurangi margin linked to fluid-rich sediments trailing subducting seamounts. *Nature Geoscience*, *16*(6), 505–512. https://doi.org/10.1038/s41561-023-01186-3

Barker, D. H. N., Henrys, S., Caratori Tontini, F., Barnes, P. M., Bassett, D., Todd, E., & Wallace, L. (2018). Geophysical constraints on the relationship between seamount subduction, slow slip, and tremor at the north Hikurangi subduction zone, New Zealand. *Geophysical Research Letters*, *45*(23), 12804–12813. https://doi.org/10.1029/2018GL080259

Barnes, J. D., Cullen, J., Barker, S., Agostini, S., Penniston-Dorland, S., Lassiter, J. C., et al. (2019). The role of the upper plate in controlling fluid-mobile element (Cl, Li, B) cycling through subduction zones: Hikurangi forearc, New Zealand. *Geosphere*, *15*(3), 642–658. https://doi.org/10.1130/GES02057.1

Barnes, P. M., Wallace, L. M., Saffer, D. M., Bell, R. E., Underwood, M. B., Fagereng, A., et al. (2020). Slow slip source characterized by lithological and geometric heterogeneity. *Science Advances*, *6*(13). https://doi.org/10.1126/sciadv.aay3314

Bell, R., Sutherland, R., Barker, D. H. N., Henrys, S., Bannister, S., Wallace, L., & Beavan, J. (2010). Seismic reflection character of the Hikurangi subduction interface, New Zealand, in the region of repeated Gisborne slow slip events. *Geophysical Journal International*, *180*(1), 34–48. https://doi.org/10.1111/j.1365-246X.2009.04401.x

Berg, R. D. (2018). *Quantifying the deep: The importance of diagenetic reactions to marine geochemical cycles* (Doctoral Dissertation). University of Washington. http://hdl.handle.net/1773/43434

Bland, K. J., Uruski, C. I., & Isaac, M. J. (2015). Pegasus Basin, eastern New Zealand: A stratigraphic record of subsidence and subduction, ancient and modern. *New Zealand Journal of Geology and Geophysics*, *58*(4), 319–343. https://doi.org/10.1080/00288306.2015.1076862

Boudreau, B. P. (1997). *Diagenetic models and their implementation: Modelling transport and reactions in aquatic sediments*. Springer-Verlag.

Brown, K. M., Saffer, D. M., & Bekins, B. A. (2001). Smectite diagenesis, pore-water freshening, and fuid flow at the toe of the Nankai wedge. *Earth and Planetary Science Letters*, *194*(1–2), 97–109. https://doi.org/10.1016/s0012-821x(01)00546-5

Chesley, C., Naif, S., Key, K., & Bassett, D. (2021). Fluid-rich subducting topography generates anomalous forearc porosity. *Nature*, *595*(7866), 255–260. https://doi.org/10.1038/s41586-021-03619-8

Crundwell, M. P., & Woodhouse, A. (2022). Biostratigraphically constrained chronologies for Quaternary sequences from the Hikurangi margin of north-eastern Zealandia. *New Zealand Journal of Geology and Geophysics*, *67*(3), 1–21. https://doi.org/10.1080/00288306.2022.2101481

Crutchley, G. J., Klaeschen, D., Henrys, S. A., Pecher, I. A., Mountjoy, J. J., & Woelz, S. (2020). Subducted sediments, upper-plate deformation and dewatering at New Zealand's southern Hikurangi subduction margin. *Earth and Planetary Science Letters*, *530*, 115945. https://doi.org/10.1016/j.epsl.2019.115945

Dragert, H., Wang, K., & James, T. S. (2001). A silent slip event on the deeper Cascadia subduction interface. *Science*, *292*(5521), 1525–1528. https://doi.org/10.1126/science.1060152

Dutilleul, J., Bourlange, S., Géraud, Y., & Stemmelen, D. (2020). Porosity, pore structure, and fluid distribution in the sediments entering the northern Hikurangi margin, New Zealand. *Journal of Geophysical Research: Solid Earth*, *125*(11), 1–21. https://doi.org/10.1029/2020JB020330

Eberhart-Phillips, D., & Bannister, S. (2015). 3-D imaging of the northern Hikurangi subduction zone, New Zealand: Variations in subducted sediment, slab fluids and slow slip. *Geophysical Journal International*, *201*(2), 838–855. https://doi.org/10.1093/gji/ggv057

Ellis, S., Fagereng, Å., Barker, D., Henrys, S., Saffer, D., Wallace, L., et al. (2015). Fluid budgets along the northern Hikurangi subduction margin, New Zealand: The effect of a subducting seamount on fluid pressure. *Geophysical Journal International*, *202*(1), 277–297. https://doi.org/10.1093/gji/ggv127

Gamage, K., & Screaton, E. (2006). Characterization of excess pore pressures at the toe of the Nankai accretionary complex, Ocean Drilling Program sites 1173, 1174, and 808: Results of one-dimensional modeling. *Journal of Geophysical Research*, *111*(B4), 1–13. https://doi.org/10.1029/2004JB003572

Gase, A. C., Bangs, N. L., Saffer, D. M., Han, S., Miller, P. K., Bell, R. E., et al. (2023). Subducting volcaniclastic-rich upper crust supplies fluids for shallow megathrust and slow slip. *Science Advances*, *9*(33), eadh0150. https://doi.org/10.1126/sciadv.adh0150

Gieskes, J., Gamo, T., & Brumsack, H. (1991). Chemical methods for interstitial water analysis aboard JOIDES resolution. *Ocean Drilling Program Technical Note*, *15*, 1–60. https://doi.org/10.2973/odp.tn.15.1991

Haeckel, M., Boudreau, B. P., & Wallmann, K. (2007). Bubble-induced porewater mixing: A 3-D model for deep porewater irrigation. *Geochimica et Cosmochimica Acta*, *71*(21), 5135–5154. https://doi.org/10.1016/j.gca.2007.08.011

Han, S., Bangs, N. L., Gase, A., Bell, R. E., Arai, R., Kodaira, S., et al. (2022). Low permeability faults inhibit fluid expulsion from the northern Hikurangi subduction margin. Presented at AGU Fall Meeting 2022, Chicago, IL.

Harris, R., Torres, M., & Solomon, E. (2023). Heat flow data from the Hikurangi subduction zone, 2019 (RR1901, RR1902) [Dataset]. *MGDS*. https://doi.org/10.26022/IEDA/331405

Heise, W., Caldwell, T. G., Bannister, S., Bertrand, E. A., Ogawa, Y., Bennie, S. L., & Ichihara, H. (2017). Mapping subduction interface coupling using magnetotellurics: Hikurangi margin, New Zealand. *Geophysical Research Letters*, *44*(18), 9261–9266. https://doi.org/10.1002/2017GL074641

Henry, P., Pichon, X. L., Lallemant, S., Lance, S., Martin, J. B., Foucher, J.-P., et al. (1996). Fluid flow in and around a mud volcano field seaward of the Barbados accretionary wedge: Results from Manon cruise. *Journal of Geophysical Research*, *101*(B9), 20297–20323.

Hensen, C., Wallmann, K., Schmidt, M., Ranero, C. R., & Suess, E. (2004). Fluid expulsion related to mud extrusion off Costa Rica - A window to the subducting slab. *Geology*, *32*(3), 201–204. https://doi.org/10.1130/G20119.1

Hensen, C., Zabel, M., Pfeifer, K., Schwenk, T., Kasten, S., Riedinger, N., et al. (2003). Control of sulfate pore-water profiles by sedimentary events and the significance of anaerobic oxidation of methane for the burial of sulfur in marine sediments. *Geochimica et Cosmochimica Acta*, *67*(14), 2631–2647. https://doi.org/10.1016/S0016-7037(03)00199-6

Hirose, H., Hirahara, K., Kimata, F., Fujii, N., & Miyazaki, S. (1999). A slow thrust slip event following the two 1996 Hyuganada earthquakes beneath the Bungo Channel, southwest Japan. *Geophysical Research Letters*, *26*(21), 3237–3240. https://doi.org/10.1029/1999GL010999

Hong, W. L., Sauer, S., Panieri, G., Ambrose, W. G., James, R. H., Plaza-Faverola, A., & Schneider, A. (2016). Removal of methane through hydrological, microbial, and geochemical processes in the shallow sediments of pockmarks along eastern Vestnesa Ridge (Svalbard). *Limnology & Oceanography*, *61*(S1), S324–S343. https://doi.org/10.1002/lno.10299

Hong, W. L., Solomon, E. A., & Torres, M. E. (2014). A kinetic-model approach to quantify the effect of mass transport deposits on pore water profiles in the Krishna-Godavari Basin, Bay of Bengal. *Marine and Petroleum Geology*, *58*(Part A), 223–232. https://doi.org/10.1016/j.marpetgeo.2014.06.014

Kastner, M., Solomon, E. A., Harris, R. N., & Torres, M. E. (2014). Fluid origins, thermal regimes, and fluid and solute fluxes in the forearc of subduction zones. In *Developments in marine geology* (Vol. 7, pp. 671–733). Elsevier. https://doi.org/10.1016/B978-0-444-62617-2.00022-0

Kluesner, J. W., Silver, E. A., Bangs, N. L., McIntosh, K. D., Gibson, J., Orange, D., et al. (2013). High density of structurally controlled, shallow to deep water fluid seep indicators imaged offshore Costa Rica. *Geochemistry, Geophysics, Geosystems*, *14*(3), 519–539. https://doi.org/10.1002/ggge.20058

Lauer, R. M., & Saffer, D. M. (2012). Fluid budgets of subduction zone forearcs: The contribution of splay faults. *Geophysical Research Letters*, *39*(13), 1–6. https://doi.org/10.1029/2012GL052182

Li, Y.-H., & Gregory, S. (1974). Diffusion of ions in sea water and in deep-sea sediments. *Geochimica et Cosmochimica Acta*, *38*(5), 703–714. https://doi.org/10.1073/pnas.1619553114

Luo, M., Hong, W. L., Torres, M. E., Kutterolf, S., Pank, K., Hopkins, J. L., et al. (2023). Volcanogenic aluminosilicate alteration drives formation of authigenic phases at the northern Hikurangi margin: Implications for subseafloor geochemical cycles. *Chemical Geology*, *619*, 121317. https://doi.org/10.1016/j.chemgeo.2023.121317

Luo, M., Yu, M., Torres, M. E., Solomon, E. A., Gieskes, J., You, C. F., et al. (2024). Volcanic ash alteration triggers active sedimentary lithium cycling: Insights from lithium isotopic compositions of pore fluids and sediments in the Hikurangi subduction zone. *Earth and Planetary Science Letters*, *642*, 118854. https://doi.org/10.1016/j.epsl.2024.118854

Martin, J. B., Kastner, M., Henry, P., Le Pichon, X., & Lallement, S. (1996). Chemical and isotopic evidence for sources of fluids in a mud volcano field seaward of the Barbados accretionary wedge. *Journal of Geophysical Research*, *101*(B9), 20325–20345. https://doi.org/10.1029/96jb00140

McCaffrey, R., Wallace, L. M., & Beavan, J. (2008). Slow slip and frictional transition at low temperature at the Hikurangi subduction zone. *Nature Geoscience*, *1*(5), 316–320. https://doi.org/10.1038/ngeo178

McNamara, D. D., Behboudi, E., Wallace, L., Saffer, D., Cook, A. E., Fagereng, A., et al. (2021). Variable in situ stress orientations across the northern Hikurangi subduction margin. *Geophysical Research Letters*, *48*(5), 1–11. https://doi.org/10.1029/2020GL091707

Moore, J. C., Brown, K. M., Horath, F., Cochrane, G., Mackay, M., & Moore, G. (1991). Plumbing accretionary prisms: Effects of permeability variations. *Philosophical Transactions of the Royal Society of London,Series A: Physical and Engineering Sciences*, *335*(1638), 275–288. https://doi.org/10.1098/rsta.1991.0047

Moore, J. C., & Vrolijk, P. (1992). Fluids in accretionary prisms. *Reviews of Geophysics*, *30*(2), 113–135. https://doi.org/10.1029/90EO00031

Morgan, J. K., Solomon, E. A., Fagereng, A., Savage, H. M., Wang, M., Meneghini, F., et al. (2022). Seafloor overthrusting causes ductile fault deformation and fault sealing along the Northern Hikurangi Margin. *Earth and Planetary Science Letters*, *593*, 117651. https://doi.org/10.1016/j.epsl.2022.117651

Mottl, M. J., Wheat, C. G., Fryer, P., Gharib, J., & Martin, J. B. (2004). Chemistry of springs across the Mariana forearc shows progressive devolatilization of the subducting plate. *Geochimica et Cosmochimica Acta*, *68*(23), 4915–4933. https://doi.org/10.1016/j.gca.2004.05.037

Nayar, K. G., Sharqawy, M. H., Banchik, L. D., & Lienhard, J. H. (2016). Thermophysical properties of seawater: A review and new correlations that include pressure dependence. *Desalination*, *390*, 1–24. https://doi.org/10.1016/j.desal.2016.02.024

Pape, T., Geprägs, P., Hammerschmidt, S., Wintersteller, P., Wei, J., Fleischmann, T., et al. (2014). Hydrocarbon seepage and its sources at mud volcanoes of the Kumano forearc basin, Nankai Trough subduction zone. *Geochemistry, Geophysics, Geosystems*, *15*(6), 2180–2194. https://doi.org/10.1002/2013GC005057

Park, J. O., Tsuru, T., Kodaira, S., Cummins, P. R., & Kaneda, Y. (2002). Splay fault branching along the Nankai subduction zone. *Science*, *297*(5584), 1157–1160. https://doi.org/10.1126/science.1074111

Peng, Z., & Gomberg, J. (2010). An integrated perspective of the continuum between earthquakes and slow-slip phenomena. *Nature Geoscience*, *3*(9), 599–607. https://doi.org/10.1038/ngeo940

Philip, B. T., Solomon, E. A., Kelley, D. S., Tréhu, A. M., Whorley, T. L., Roland, E., et al. (2023). Fluid sources and overpressures within the central Cascadia Subduction Zone revealed by a warm, high-flux seafloor seep. *Science Advances*, *9*(4). https://doi.org/10.1126/sciadv.add6688

Ranero, C. R., Grevemeyer, I., Sahling, H., Barckhausen, U., Hensen, C., Wallmann, K., et al. (2008). Hydrogeological system of erosional convergent margins and its influence on tectonics and interplate seismogenesis. *Geochemistry, Geophysics, Geosystems*, *9*(3). https://doi.org/10.1029/2007GC001679

Reyes, A. G., Christenson, B. W., & Faure, K. (2010). Sources of solutes and heat in low-enthalpy mineral waters and their relation to tectonic setting, New Zealand. *Journal of Volcanology and Geothermal Research*, *192*(3–4), 117–141. https://doi.org/10.1016/j.jvolgeores.2010.02.015

Sacks, S. I., Suyehiro, S., Linde, A. T., & Snoke, J. A. (1978). Slow earthquakes and stress redistribution. *Nature*, *275*(5681), 599–602. https://doi.org/10.1038/275599a0

Saffer, D. M., & Bekins, B. A. (1998). Episodic fluid flow in the Nankai accretionary complex: Timescale, geochemistry, flow rates, and fluid budget. *Journal of Geophysical Research*, *103*(B12), 30351–30370. https://doi.org/10.1029/98JB01983

Saffer, D. M., & Screaton, E. J. (2003). Fluid flow at the toe of convergent margins: Interpretation of sharp pore-water geochemical gradients. *Earth and Planetary Science Letters*, *213*(3–4), 261–270. https://doi.org/10.1016/S0012-821X(03)00343-1

Saffer, D. M., & Tobin, H. J. (2011). Hydrogeology and mechanics of subduction zone forearcs: Fluid flow and pore pressure. *Annual Review of Earth and Planetary Sciences*, *39*(1), 157–186. https://doi.org/10.1146/annurev-earth-040610-133408

Saffer, D. M., & Wallace, L. M. (2015). The frictional, hydrologic, metamorphic and thermal habitat of shallow slow earthquakes. *Nature Geoscience*, *8*, 594–600. https://doi.org/10.1038/ngeo2490

Scholz, F., Hensen, C., Schmidt, M., & Geersen, J. (2013). Submarine weathering of silicate minerals and the extent of pore water freshening at active continental margins. *Geochimica et Cosmochimica Acta*, *100*, 200–216. https://doi.org/10.1016/j.gca.2012.09.043

Schwartz, S. Y., & Rokosky, J. M. (2007). Slow slip events and seismic tremor at circum-Pacific subduction zones. *Reviews of Geophysics*, *45*(3), 1–32. https://doi.org/10.1029/2006RG000208.1

Shaddox, H. R., & Schwartz, S. Y. (2019). Subducted seamount diverts shallow slow slip to the forearc of the northern Hikurangi subduction zone, New Zealand. *Geology*, *47*(5), 415–418. https://doi.org/10.1130/G45810.1

Sharqawy, M. H., Lienhard, J. H., & Zubair, S. M. (2010). Thermophysical properties of seawater: A review of existing correlations and data. *Desalination and Water Treatment*, *16*(1–3), 354–380. https://doi.org/10.5004/dwt.2010.1079

Sibson, R. H. (1990). Conditions for fault-valve behaviour. *Geological Society, London, Special Publications*, *54*(1), 15–28. https://doi.org/10.1144/GSL.SP.1990.054.01.02

Sibson, R. H., & Rowland, J. V. (2003). Stress, fluid pressure and structural permeability in seismogenic crust, North Island, New Zealand. *Geophysical Journal International*, *154*(2), 584–594. https://doi.org/10.1046/j.1365-246X.2003.01965.x

Solomon, E. A., Kastner, M., Jannasch, H., Robertson, G., & Weinstein, Y. (2008). Dynamic fluid flow and chemical fluxes associated with a seafloor gas hydrate deposit on the northern Gulf of Mexico slope. *Earth and Planetary Science Letters*, *270*(1–2), 95–105. https://doi.org/10.1016/j.epsl.2008.03.024

Solomon, E. A., Kastner, M., Wheat, C. G., Jannasch, H., Robertson, G., Davis, E. E., & Morris, J. D. (2009). Long-term hydrogeochemical records in the oceanic basement and forearc prism at the Costa Rica subduction zone. *Earth and Planetary Science Letters*, *282*(1–4), 240–251. https://doi.org/10.1016/j.epsl.2009.03.022

Stein, J. S., & Fisher, A. T. (2001). Multiple scales of hydrothermal circulation in Middle Valley, northern Juan de Fuca Ridge: Physical constraints and geologic models. *Journal of Geophysical Research*, *106*(B5), 8563–8580. https://doi.org/10.1029/2000jb900395

Sun, T., Ellis, S., & Saffer, D. (2020). Coupled evolution of deformation, pore fluid pressure, and fluid flow in shallow subduction forearcs. *Journal of Geophysical Research: Solid Earth*, *125*(3), 1–26. https://doi.org/10.1029/2019JB019101

Sun, T., Saffer, D., & Ellis, S. (2020). Mechanical and hydrological effects of seamount subduction on megathrust stress and slip. *Nature Geoscience*, *13*(3), 249–255. https://doi.org/10.1038/s41561-020-0542-0

Toki, T., Higa, R., Ijiri, A., Tsunogai, U., & Ashi, J. (2014). Origin and transport of pore fluids in the Nankai accretionary prism inferred from chemical and isotopic compositions of pore water at cold seep sites off Kumano. *Earth Planets and Space*, *66*(137), 1–14. https://doi.org/10.1186/s40623-014-0137-3

Torres, M. E., Teichert, B. M. A., Tréhu, A. M., Borowski, W., & Tomaru, H. (2004). Relationship of pore water freshening to accretionary processes in the Cascadia margin: Fluid sources and gas hydrate abundance. *Geophysical Research Letters*, *31*(22), 1–4. https://doi.org/10.1029/2004GL021219

Tryon, M. D., Brown, K. M., Torres, M. E., Tréhu, A. M., McManus, J., & Collier, R. W. (1999). Measurements of transience and downward fluid flow near episodic methane gas vents, Hydrate Ridge, Cascadia. *Geology*, *27*(12), 1075–1078. https://doi.org/10.1130/0091-7613(1999)027<1075:MOTADF>2.3.CO;2

Tryon, M. D., Wheat, C. G., & Hilton, D. R. (2010). Fluid sources and pathways of the Costa Rica erosional convergent margin. *Geochemistry, Geophysics, Geosystems*, *11*(4), 1–15. https://doi.org/10.1029/2009GC002818

Vasseur, G., Demongodin, L., & Bonneville, A. (1993). Thermal modelling of fluid flow effects in thin-dipping aquifers. *Geophysical Journal International*, *112*(2), 276–289. https://doi.org/10.1111/j.1365-246X.1993.tb01455.x

Villinger, H., & Davis, E. E. (1987). A new reduction algorithm for marine heat flow measurements. *Journal of Geophysical Research*, *92*(B12), 12846–12856. https://doi.org/10.1029/jb092ib12p12846

Wallace, L. M. (2020). Slow slip events in New Zealand. *Annual Review of Earth and Planetary Sciences*, *48*(1), 175–203. https://doi.org/10.1146/annurev-earth-071719-055104

Wallace, L. M., Saffer, D. M., Barnes, P. M., Pecher, I. A., Petronotis, K. E., & LeVay, L. J. (2019). Hikurangi subduction margin coring, logging, and observatories. *Proceedings of the International Ocean Discovery Program*, *372B/375*. https://doi.org/10.14379/iodp.proc.372B375.2019

Wallace, L. M., Webb, S. C., Ito, Y., Mochizuki, K., Hino, R., Henrys, S., et al. (2016). Slow slip near the trench at the Hikurangi subduction zone, New Zealand. *Science*, *352*(6286), 701–704. https://doi.org/10.1126/science.aaf2349

Warren-Smith, E., Fry, B., Wallace, L., Chon, E., Henrys, S., Sheehan, A., et al. (2019). Episodic stress and fluid pressure cycling in subducting oceanic crust during slow slip. *Nature Geoscience*, *12*(6), 475–481. https://doi.org/10.1038/s41561-019-0367-x

Watson, S. J., Mountjoy, J. J., Barnes, P. M., Crutchley, G. J., Lamarche, G., Higgs, B., et al. (2020). Focused fluid seepage related to variations in accretionary wedge structure, Hikurangi margin, New Zealand. *Geology*, *48*(1), 56–61. https://doi.org/10.1130/G46666.1

Zal, H. J., Jacobs, K., Savage, M. K., Yarce, J., Mroczek, S., Graham, K., et al. (2020). Temporal and spatial variations in seismic anisotropy and VP/VS ratios in a region of slow slip. *Earth and Planetary Science Letters*, *532*, 115970. https://doi.org/10.1016/j.epsl.2019.115970